Analysis of Wide-Band Stripline Circulators by Integral Equation Technique

YALCIN AYASLI

Abstract—**The analysis of wide-band Y-junction stripline circulators using Green's function method was reported in the literature. In this paper, similar analyses are performed using an integral equation method and the results are compared.**

The boundary conditions used in the analyses are also discussed. A new boundary condition representing the actual fields more precisely than previously is formulated and applied to the junction. The results obtained with the new boundary conditions are examined and compared with the previous theoretical and experimental results.

The current and voltage distributions that are created at the ports under the assumed boundary conditions are calculated and compared with the known stripline and junction modes.

In the formulation, it is observed that the Green's function is not unique and it can be selected from a certain class of functions. This arbitrariness is introduced into the formulation by means of a complex parameter C_0. The effect of this parameter on the numerical results is investigated and it is shown that in certain regions of the complex C_0 plane, the numerical results converge on the analytical results.

I. Introduction

WU AND Rosenbaum [1] proposed the concept of intrinsically wide-band stripline circulators and experimentally verified this with a 7–14 GHz octave band design in 1974. Later, Ayter and Ayasli [2] reported the design of another wide-band circulator at 2–4 GHz using frequency-independent design curves. They also calculated and compared the theoretical responses of both 2–4 and 7–14 GHz designs using Green's function technique.

In this paper, the theoretical performance of the two wide-band designs mentioned above are examined by the integral equation technique [3]. In this examination, the boundary conditions are chosen consistent with the Green's function analysis to allow comparison with the previous Ayter–Ayasli results [2]. The validity of these boundary conditions are then investigated and a new set which approximates the real distributions better is introduced. The new set of boundary conditions are applied to the junction and the results are compared with the previous results.

The integral equation method is especially suitable for the analysis of arbitrary shaped planar microwave circuits. In the application of the method to such circuits, the free space Green's function has been consistently used [3], [4].

Manuscript received June 6, 1979; revised October 17, 1979.

Y. Ayasli was with the Department of Electrical Engineering, Middle East Technical University, Ankara, Turkey. He is now with the Raytheon Research Division, Waltham, MA, on leave of absence from the Middle East Technical University.

In this paper it is pointed out that the Green function suitable to the integral equation method is not unique and, in fact, can be chosen from a certain class of functions. This arbitrariness in the Green's function is also investigated and its effect on the accuracy and convergence of the numerical results is examined.

II. Integral Equation Formulation

For the junction geometry shown in Fig. 1 and when the thickness of the ferrite is much less than the wavelength, the fields in the junction can be taken as independent of z. Then only the z component of the electric field can exist and it should satisfy the wave equation.

$$\frac{\partial^2 E_z}{\partial r^2}+\frac{1}{r}\frac{\partial E_z}{\partial r}+\frac{1}{r^2}\frac{\partial^2 E_z}{\partial \theta^2}+k^2 E_z=0 \tag{1}$$

where

$k^2=\omega^2\epsilon_0\epsilon_f\mu_{\text{eff}}$	radial wave propagation constant
$\mu_{\text{eff}}=(\mu^2-\kappa^2)/\mu$	effective permeability of the ferrite
μ,κ	Polder tensor elements.

Following the analysis of Miyoshi *et al.* [3], the electric field E_z at some point $\bar{r}_M$ on the circumference of the junction is given by

$$E_z(\bar{r}_M)=2\oint_c j\omega\mu_{\text{eff}}G(kR)H_l(\bar{r}_0)dl$$

$$-2\oint_c\left(\cos\theta_0-j\frac{\kappa}{\mu}\sin\theta_0\right)\frac{\partial G(kR)}{\partial R}E_z(\bar{r}_0)dl. \tag{2}$$

Contour C and the quantities such as $\bar{r}_M$, $\bar{r}_0$, and θ_0 are shown in Fig. 2. If the tangential magnetic field component $H_l(\bar{r}_0)$ is assumed to be known along C, then (2) is a Fredholm integral equation in terms of E_z. $G(kR)$, in this equation is the two-dimensional Green's function and can be expressed in the most general form as

$$G(kR)=C_0J_0(kR)-\frac{1}{4}Y_0(kR) \tag{3}$$

where

C_0	a complex constant
R	$=\lvert\bar{r}_M-\bar{r}_0\rvert$
$J_0(kR)$	first kind zeroth-order Bessel function
$Y_0(kR)$	second kind zeroth-order Bessel function.

In (3), the coefficient of $Y_0(kR)$ is determined to be $-1/4$ from the singularity condition at $R=0$. Because there is no other condition imposed on $G(kR)$, the constant C_0

0018-9480/80/0300-0200$00.75 ©1980 IEEE

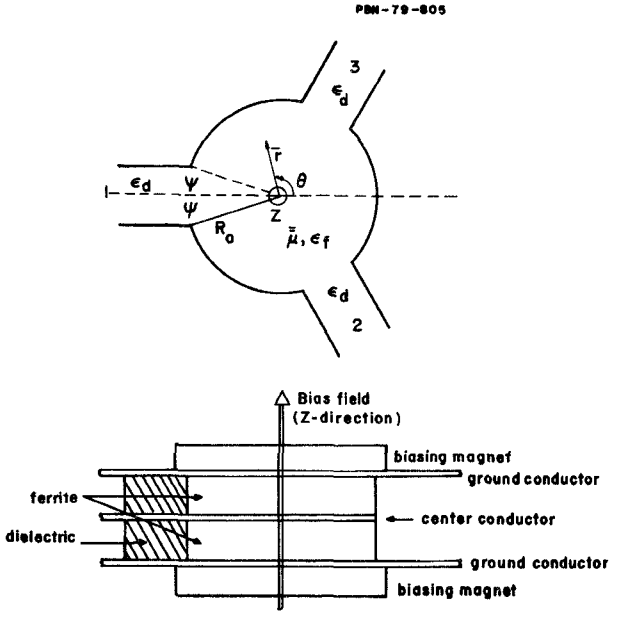

Fig. 1. Junction geometry. (a) Top view. (b) Cross section.

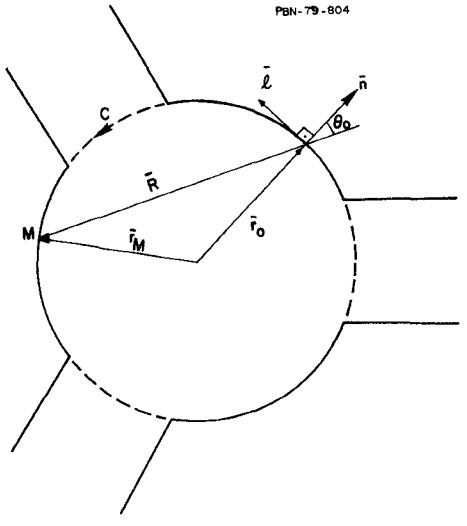

Fig. 2. Contour C and related coordinates.

should be able to take any value (which could be complex due to the assumed $e^{(j\omega t)}$ dependence).

In the literature [3], [4] C_0 is taken as $-j/4$ which reduces (3) to the free space Green's function as

$$G(kR) = -jH_0^{(2)}(kR)/4 \tag{4}$$

where $H_0^{(2)}(kR)$ is the second kind zeroth-order Hankel function.

Analytically one can readily show that the solution for $E_z(\bar{r}_M)$ is independent of C_0. However, these equations are solved numerically and not analytically. To obtain a numerical solution, the integral equation is reduced to a finite size matrix equation. In this transformation truncation errors occur due to the finite matrix size used. In addition, the usual sources of error peculiar to the numerical solutions are present. Thus the numerical solutions are only an approximation to the analytical solutions and the effect of the parameter C_0 on these numerical solutions is not obvious. The effect of C_0 on the numerical results is discussed in Appendix A.

III. Numerical Formulation

For the numerical evaluation of the integral equation (2), the contour C can be divided into N equal segments. If N is large enough, the length of the segments will be small and the fields existing in the junction can be taken as constant along each segment.

Total length of contour C is about a wavelength in the operation band and, as an example, choosing $N=36$ would correspond to sampling a sine wave at 10° intervals.

If the contour integral is thought of as the sum of N line integrals over an interval w, (2) can be written as

$$e_i = j2\omega\mu_{\text{eff}} \sum_{j=1}^{N} h_j \int_{w_j} G(kR_{ij})\,dl_j - \sum_{j=1}^{N} 2ke_j \int_{w_j} \left(\cos\theta_{ij} - j\frac{\kappa}{\mu}\sin\theta_{ij}\right) G'(kR_{ij})\,dl_j. \tag{5}$$

In this equation, e_i is the value of E_z at the ith segment and h_j is the value of H_t at the jth segment. Because e_i and h_j are taken to be constant, they are taken outside the integrations.

Equation (5) can be expressed as

$$\sum_{j=1}^{N} U_{ij}e_j = \sum_{j=1}^{N} T_{ij}h_j, \qquad i = 1,2,\cdots,N \tag{6}$$

or as

$$[U][e] = [T][h]. \tag{7}$$

Comparing (5) and (6),

$$U_{ij} = \delta_{ij} + 2k \int_{w_j} \left(\cos\theta_{ij} - j\frac{\kappa}{\mu}\sin\theta_{ij}\right) G'(kR_{ij})\,dl_j \tag{8}$$

and

$$T_{ij} = j2\omega\mu_{\text{eff}} \int_{w_j} G(kR_{ij})\,dl_j \tag{9}$$

are found. If the h_j's are assumed to be known around the junction circumference, then the e_j's can be calculated from (6).

IV. Application of the Method to Wide-Band Designs and Boundary Conditions

Wide-band designs operate in the approximate octave band $f_z + f_m < f < 2f_m$. The designs require that the coupling angle 2Ψ is chosen as equal or wider than 60°. The angle 2Ψ is chosen as 60°, 65°, and 75° in references [1], [2], and [5], respectively. As a result of wide coupling angle, when the circulator circumference is divided into N segments, more than one sampling point falls into the input ports. As an example, for Wu–Rosenbaum [1] design, the junction circumference and the sampling points are shown in Fig. 3, if $N=36$. The boundary conditions on the junction are discussed in terms of this example.

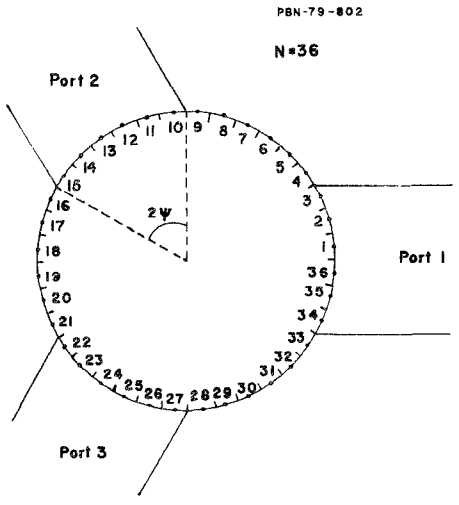

Fig. 3. Junction geometry and sampling points for Wu–Rosenbaum design and $N=36$.

A. Constant Magnetic Field at the Ports

The boundary condition used in the Green's function analysis can be expressed in terms of complex constants a, b, and c as in [6]

$$H_l=\begin{cases} a, & \text{in port 1} \\ b, & \text{in port 2} \\ c, & \text{in port 3} \\ 0, & \text{elsewhere.} \end{cases} \tag{10}$$

The electric field E_z at the ports then comes out as a function of the θ variable and by averaging it along a portwidth, an equivalent electric field is defined.

To be able to compare the results of the integral equation analysis with the results of the Green's function analysis, boundary conditions similar to the ones expressed in (10) are applied first. In terms of the tangential magnetic fields at the sampling points and referring to the numbers in Fig. 3, boundary conditions equivalent to (10) become

$$\begin{aligned} a &= h_1 = h_2 = h_3 = h_{34} = h_{35} = h_{36} \\ b &= h_{10} = h_{11} = h_{12} = h_{13} = h_{14} = h_{15} \\ c &= h_{22} = h_{23} = h_{24} = h_{25} = h_{26} = h_{27}. \end{aligned} \tag{11}$$

The average electric fields E_1, E_2, and E_3 at the ports can then be calculated as

$$\begin{aligned} E_1 &= (e_1+e_2+e_3+e_{34}+e_{35}+e_{36})/6 \\ E_2 &= (e_{10}+e_{11}+e_{12}+e_{13}+e_{14}+e_{15})/6 \\ E_3 &= (e_{22}+e_{23}+e_{24}+e_{25}+e_{26}+e_{27})/6. \end{aligned} \tag{12}$$

These average field quantities defined at the ports are also related through the scattering matrix

$$S=\begin{bmatrix} \alpha & \beta & \gamma \\ \gamma & \alpha & \beta \\ \beta & \gamma & \alpha \end{bmatrix} \tag{13}$$

of the junction. If it is assumed that the junction is excited from port 1 and the other ports are terminated by matched loads, the average field quantities are [6]

$$\begin{aligned} a &= (1-\alpha)a^+ \\ b &= -\beta a^+ \\ c &= -\gamma a^+ \end{aligned} \tag{14}$$

and

$$\begin{aligned} E_1 &= Z_d(1+\alpha)a^+ \\ E_2 &= Z_d\beta a^+ \\ E_3 &= Z_d\gamma a^+. \end{aligned} \tag{15}$$

In these equations a^+ represents the incident average magnetic field H_l at port 1 and Z_d is the wave impedance of the input stripline. Without losing any generality a^+ can be taken as unity and from (14) and (15):

$$\begin{aligned} a &= 2-E_1/Z_d \\ b &= -E_2/Z_d \\ c &= -E_3/Z_d. \end{aligned} \tag{16}$$

When (16) is combined with (7), N equations with the electric fields e_i as unknowns result. If this system of equations is expressed as a matrix equation in the form of

$$[U'][e]=[R] \tag{17}$$

then, for the example of Fig. 3,

$$\begin{aligned} U'(I,J) &= U(I,J)+[T(I,1)+T(I,2)+T(I,3) \\ &\quad +T(I,34)+T(I,35)+T(I,36)]/6Z_d, \\ &\quad J=1,2,3,34,35,36,\ I=1,2,\cdots,36 \end{aligned} \tag{18a}$$

$$\begin{aligned} U'(I,J) &= U(I,J)+[T(I,10)+T(I,11)+T(I,12) \\ &\quad +T(I,13)+T(I,14)+T(I,15)]/6Z_d, \\ &\quad J=10,11,12,13,14,15,\ I=1,2,\cdots,36 \end{aligned} \tag{18b}$$

$$\begin{aligned} U'(I,J) &= U(I,J)+[T(I,22)+T(I,23)+T(I,24) \\ &\quad +T(I,25)+T(I,26)+T(I,27)]/6Z_d, \\ &\quad J=22,23,24,25,26,27,\ I=1,2,\cdots,36 \end{aligned} \tag{18c}$$

and

$$\begin{aligned} R(I) &= 2[T(I,1)+T(I,2)+T(I,3)+T(I,34) \\ &\quad +T(I,35)+T(I,36)], \qquad I=1,2,\cdots,36 \end{aligned} \tag{19}$$

can be written.

From the solution of (17), the electric field E_z sampled at 36 points along the junction circumference can be found. Using these fields, the scattering matrix elements α, β, and γ can be found as

$$\begin{aligned} \alpha &= (e_1+e_2+e_3+e_{34}+e_{35}+e_{36})/6Z_d-1 \\ \beta &= (e_{10}+e_{11}+e_{12}+e_{13}+e_{14}+e_{15})/6Z_d \\ \gamma &= (e_{22}+e_{23}+e_{24}+e_{25}+e_{26}+e_{27})Z_d. \end{aligned} \tag{20}$$

The performance of the junction as a circulator can then be calculated as

$$\begin{aligned} \text{Return loss} &= 20\log_{10}|\alpha| \\ \text{Insertion loss} &= 20\log_{10}|\beta| \\ \text{Isolation} &= 20\log_{10}|\gamma|. \end{aligned} \tag{21}$$

B. Constant Electric Field at the Ports

For the Green's function analysis, the boundary conditions given in (10) are the most convenient to apply. But they do not truly represent the actual field distributions at the ports.

The TEM voltage and current distributions that exist on a stripline [7] are shown in Fig. 4. Since no z-variation for the fields is assumed, then H_t and E_z should have distributions similar to current and voltage distributions, respectively. In the region where the ports joint the junction, however, higher order modes exist and modify these distributions. In spite of this, the distributions in Fig. 4 suggest that taking the electric field distribution as constant and letting the magnetic field distribution free for any value it takes seems more meaningful. Thus a new and more realistic boundary condition is

$$E_z = \begin{cases} E_1, & \text{in port 1} \\ E_2, & \text{in port 2} \\ E_3, & \text{in port 3} \end{cases} \tag{22}$$

and

$$H_t = 0, \qquad \text{outside the ports.} \tag{23}$$

Using (22) and (23) instead of (10) and following a similar routine, a matrix equation of the form (17) can be obtained. Due to the mixed boundary conditions used, however, the unknowns of the problem become the tangential magnetic field at the ports and the electric field outside the ports.

V. Numerical Results

The integral equation method is used for the analysis of two wide-band circulator designs reported in the literature [1], [2]. For each design, two different sets of boundary conditions described above are separately examined for $C_0 = +300$ (see Appendix A for the choice of C_0).

The resonant frequencies of the disk-shaped circuit is calculated first to check the computational accuracy. The equation which gives the resonance frequencies is

$$\det[U] = 0. \tag{24}$$

Due to computational errors, (24) is not completely satisfied and the frequencies which give the minimum of $|\det[U]|$ can be taken as the eigenvalues [3]. The exact eigenvalues, on the other hand are the roots of

$$|J_n'(kR_0)| - \left| \frac{\kappa}{\mu} \frac{nJ_n(kR_0)}{kR_0} \right| = 0, \qquad n = 0, 1, 2, \cdots . \tag{25}$$

Thus the exact and calculated resonance frequencies can be compared giving information on the computational errors involved. From this comparison, it is found that for $N = 33$, $H_i = 3300$ Oe, $4\pi M_s = 1300$ G, $R_0 = 0.0039$ m, and $C_0 = -j/4$, the difference between the exact and calculated frequencies is less than 0.15 percent. For similar parameters, Miyoshi *et al.* [3] reports a 2-percent computational error. This improvement in the accuracy of the numerical results is achieved by using (8) and (9) instead of the approximate expressions in the calculation of diagonal terms for the $[U]$ and $[T]$ matrices.

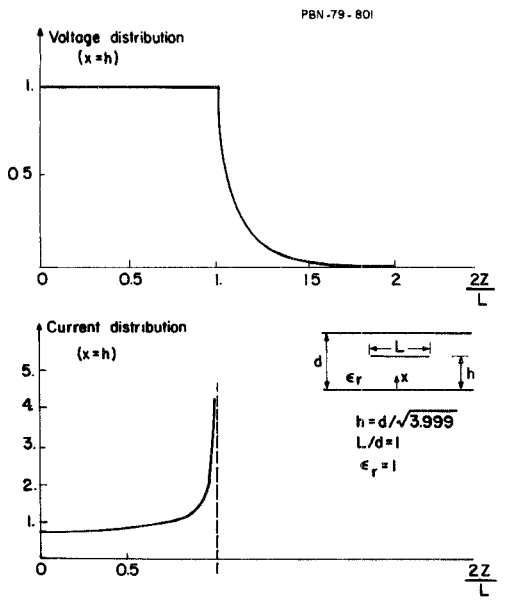

Fig. 4. Calculated voltage and current distributions on a typical stripline configuration (in relative units) [7].

A. Constant Magnetic Field at the Ports

The numerical results obtained for the Wu–Rosenbaum design [1] with constant magnetic field boundary condition at the ports are shown in Fig. 5. On the same figure the results obtained with the Green's function analysis [2] are also shown for comparison.

The results obtained by the two different methods are in good agreement. In the analysis of reference [2], the Green's function is calculated by using the first three terms of the infinite series expansion; therefore, a wider resonance is not surprising. The degradation in the performance of the junction around 13.4 GHz is present in both results.

The integral equation technique is also applied to Ayter–Ayasli design [2] and the results are shown in Fig. 6 together with the results of the Green's function analysis. In this application, the contour C is divided into 30 equal segments with 6 sampling points left for each port. This sets $\Psi = 0.628$ rads. The actual Ψ used in the design is 0.646 rad. The difference between the coupling angles Ψ used in the two methods of analysis makes point by point comparison difficult and causes the offset in the center frequencies seen in Fig. 6. The general shape of the curves are, however, in agreement.

B. Constant Electric Field at the Ports

The two wide-band designs of the previous section are also investigated using the constant electric field boundary condition. The results are shown in Figs. 7 and 8. The shift to higher frequencies seen in Fig. 8 should be due to the slightly different Ψ value used in the model.

Comparing Figs. 7, 8 and 5, 6, respectively, a general decrease in isolation and a general increase in insertion loss are observed. Although the reported experimental

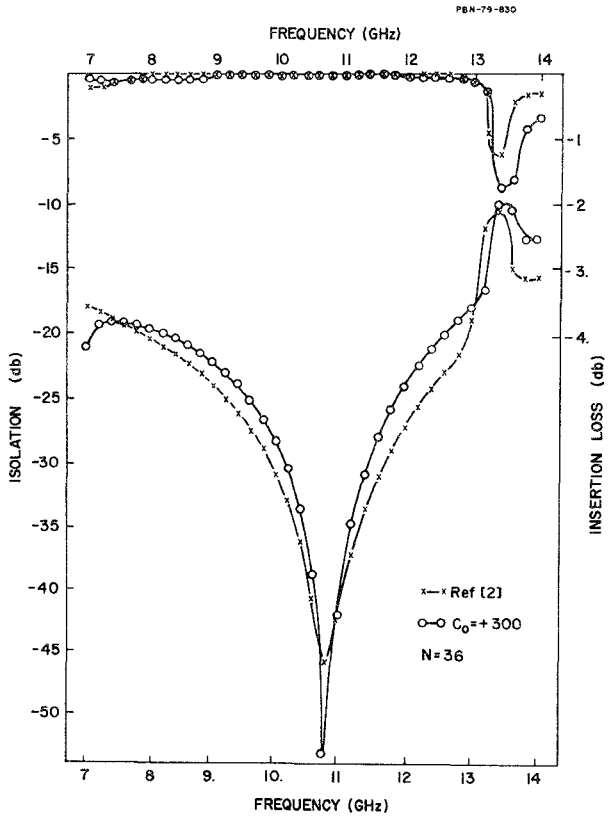

Fig. 5. Comparison of integral equation and Green's function results for Wu–Rosenbaum design with constant magnetic field boundary condition.

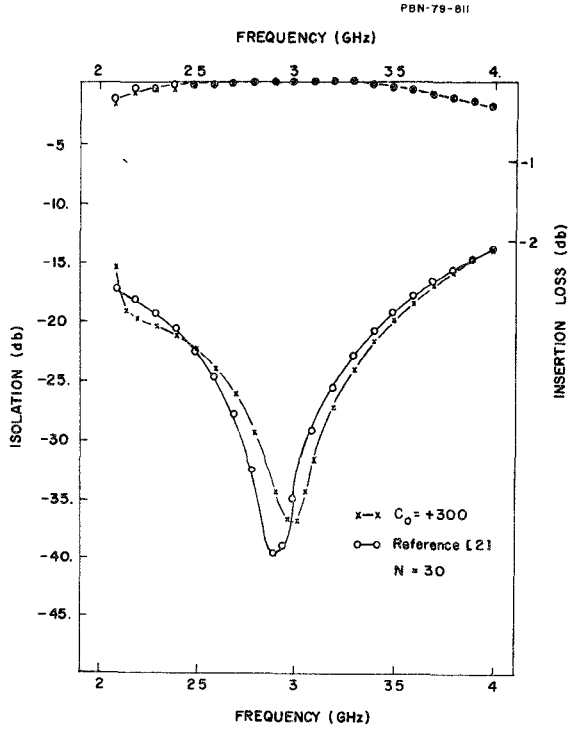

Fig. 6. Comparison of integral equation and Green's function results for Ayter–Ayasli design with constant magnetic field boundary condition.

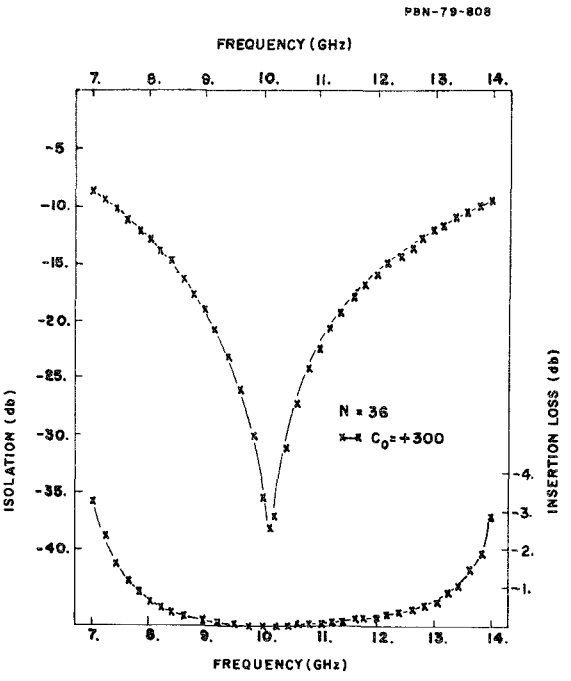

Fig. 7. Integral equation results for Wu–Rosenbaum design with constant electric field boundary condition.

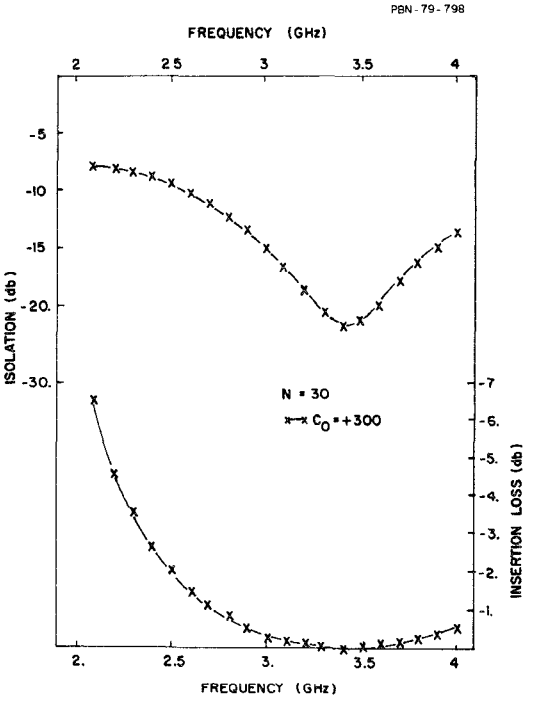

Fig. 8. Integral equation results for Ayter–Ayasli design with constant electric field boundary condition.

results [1], [2] include the effect of the matching sections and thus cannot be directly compared with the curves of Figs. 7 and 8, these observed tendencies improve the agreement between the experimental and calculated constant electric field boundary condition results.

The boundary conditions require $H_t = 0$ outside the ports, when actually fringing fields exist there. The effect

of these fringing fields is included in the model by defining an effective disk radius as [3]

$$R_{\text{eff}} = R_0 + 0.1788 \times D \tag{26}$$

where D is the ferrite disk thickness. To allow comparison with the previous results [2], this correction was not made for the results of Figs. 5 and 6. If this correction were made for these figures, the center frequencies would move to 9.6 GHz and 2.65 GHz, respectively.

C. Calculated Field Distributions at the Ports

In comparing the results obtained with the two different boundary conditions, it is also instructive to examine the field distributions which form at the ports, checking whether or not they violate any of the previous assumptions.

In Fig. 9, the electric field distributions at the ports are shown for the Wu–Rosenbaum design [1] with the constant magnetic field boundary condition. On the other hand, the magnetic field distributions for the same design with constant electric field boundary condition are shown in Fig. 10. In both figures, the distributions are calculated at the center frequencies.

To be able to interpret these distributions better, the modes that exist in the junction are shown in Fig. 11 [6]. From the examination of these modes, it is clear that fields must have symmetry only with respect to the isolated port (port 3). At the other ports, the fields are not symmetric with respect to the port center, and instead increase in the direction away from the isolated port.

In Figs. 9 and 10, the calculated field distributions agree with the qualitative discussion above. In the isolated port (port 3), however, since the sum of the two junction modes results in a null field, the electric and magnetic field distributions must be determined by the stripline mode. The magnetic field distribution at port 3 in Fig. 10 is in good agreement with the current distribution in Fig. 4. The electric field distribution at port 3 in Fig. 9, however, disagrees with the voltage distribution in Fig. 4, the same way the constant magnetic field boundary condition disagrees with the current distribution in the same figure.

VI. Conclusion

The integral equation method is applied to the analysis of wide-band circulators. In this analysis, the junction is first modeled with boundary conditions similar to the conditions used in the previous Green's function analysis [2]. The results obtained by these two different methods are then compared. This comparison shows that the results are in agreement.

In the integral equation analysis, it is noted that a more realistic boundary condition can be formulated and applied to the junction. The results obtained with the different boundary conditions are then compared, showing that the new boundary condition increases the agreement between the theoretical and experimental results.

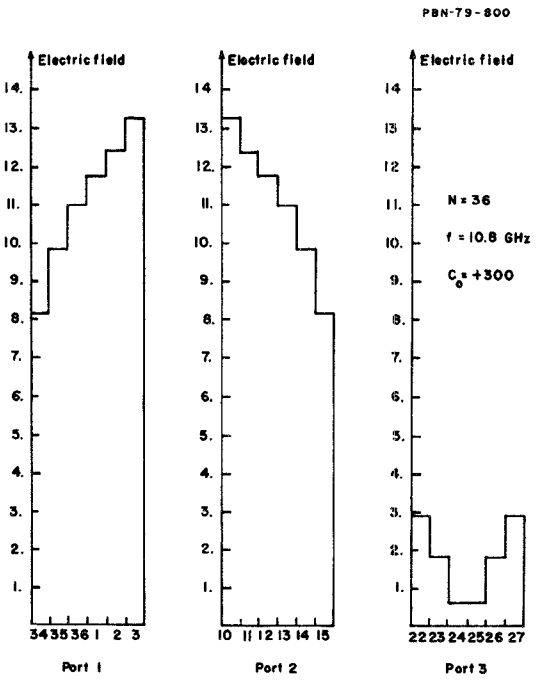

Fig. 9. Calculated electric field distribution at the ports for Wu–Rosenbaum design with constant magnetic field boundary condition (in relative units).

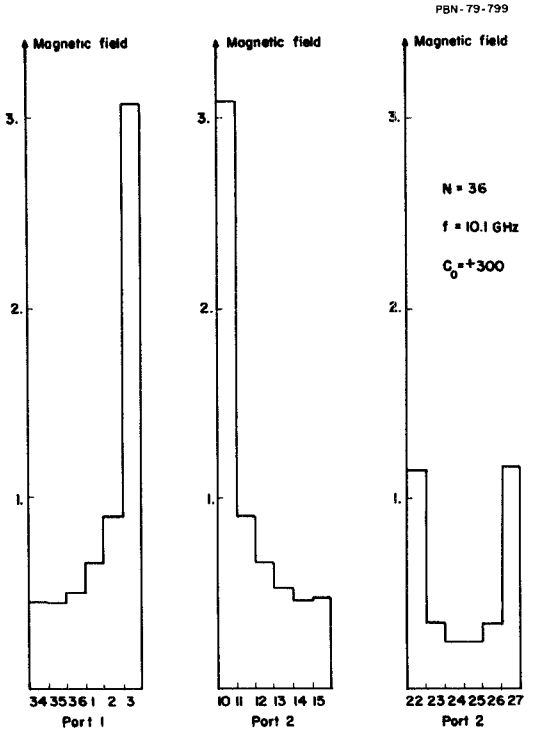

Fig. 10. Calculated magnetic field distribution at the ports for Wu–Rosenbaum design with constant electric field condition (in relative units).

The theoretical circulator performance obtained for the Wu–Rosenbaum design [1] with constant electric field boundary condition does not show any deterioration at 13.4 GHz as observed in both Green's function and integral equation results with constant magnetic field

boundary condition. This means that the deterioration is an effect strictly due to the constant magnetic field boundary condition used.

The magnetic or electric field distributions created at the ports under two different boundary conditions are also calculated and compared with the modes of the junction and of the stripline. From this comparison, it is observed that only the constant electric field boundary condition at the ports does not lead to any inconsistencies.

For analyses based on the solution of integral equations in the form of (2), it is shown that an arbitrary parameter C_0 can be introduced into the Green's function used. The physical results should ideally be independent of this parameter and there are no *a priori* criteria which dictates a certain choice for it. The integral equation is then transformed to a finite size matrix equation and the effect of this parameter on the numerical solutions is investigated.

The computer results of this investigation show that by finding a region where the results are independent of C_0, the difference between the numerical and theoretical results can be decreased and a convergence between them can be obtained. In this region of convergence, the numerical results become independent of the number of equations used and thus a minimum number of equations showing a C_0 independent region in their solution can be used.

The numerical results also indicate that in the process of increasing C_0 to find a region of convergence, the stability of the matrix equations decreases linearly with C_0. However, while the condition number of the system is increasing steadily to rather large values, very little change is observed in the numerical results. Clearly, a compromise seems possible for the proper choice of C_0. The convergence obtained through the arbitrariness of C_0 is a property of the integral equation formulation and thus its application is not limited to two-dimensional problems.

Appendix A

In this appendix, the effect of the parameter C_0 on the numerical results is investigated. In Fig. 12, the calculated values of the first resonance frequency for $N=33$, $R_0=0.0039$ m, $H_i=3300$ Oe, and $4\pi M_s=1300$ G are plotted for several values of C_0 as it is varied along the $\pm$real axes. From this figure, it is seen that as C_0 is increased, the frequencies obtained from the minimum of $|\det[U]|$ converge on the exact value of 4.37080 GHz calculated from (25) for $n=1$. Six significant number accuracy is the limit of the Bessel's function expansions and the single precision calculations used.

In Section II, it is pointed out that the physical results, when obtained analytically, should be independent of C_0. But the integral equation is solved numerically by transforming it to a finite set of linear equations. As a result of this transformation, the more numerical solutions converge to the exact integral equation solutions, the less they should depend on the parameter C_0.

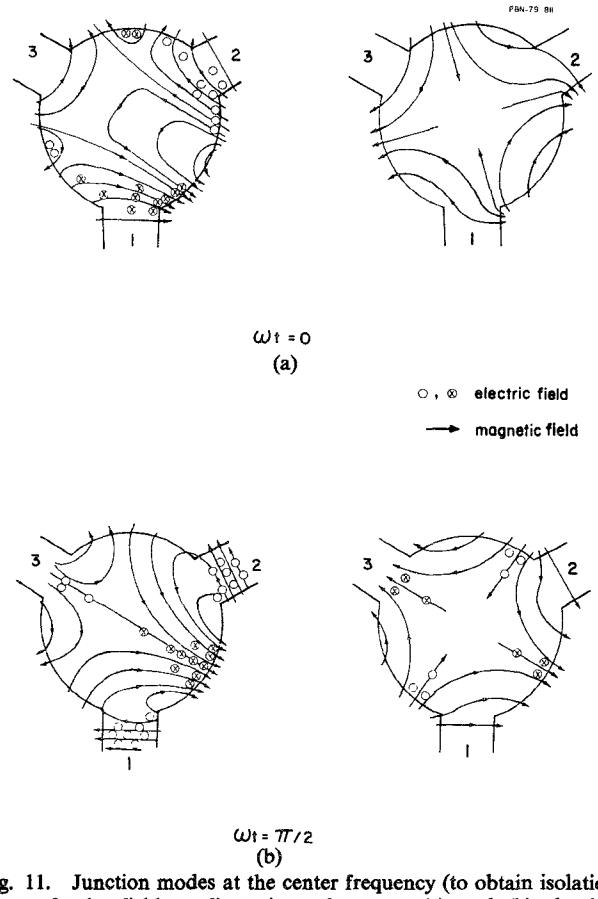

Fig. 11. Junction modes at the center frequency (to obtain isolation at port 3, the field configurations shown at (a) and (b) should be superimposed) [6].

In Fig. 13, the effect of C_0 on the diagonal element of the scattering matrix is shown for the Ayter–Ayasli design at a single frequency. This figure shows that as C_0 is increased along the $\pm$real and $\pm$imaginary axes on the complex C_0 plane, the magnitude of α converges to a certain value. Convergence occurs fastest on the real C_0 axis. After convergence is reached, as C_0 is varied in a rather large region from $+50$ to $+1000$, $|\alpha|$ changes only 2 percent.

In Fig. 14, the variation of $|\alpha|$ with C_0 as the latter is varied along the $+$real is shown for the four cases mentioned in Section V. For these four cases, the convergence is clearly seen for C_0 larger than $+200$. Above this value, the results are nearly independent of C_0. This independence means that in this C_0 region, the numerical results behave as expected from the analytical solutions and thus the matrix equation is modeling the junction properly.

In Figs. 13 and 14, the variation of $|\alpha|$ with the parameter C_0 are shown only at one frequency near midband. To see if the convergence obtained for certain C_0 values is sensitive to the parameters of the model, the behavior of the circulator for one of the four cases above is shown in Fig. 15 over the entire frequency band for two different values of C_0. From this figure, it is seen that the results for $C_0=+300$ and $C_0=+500$ are in close agreement over the band of operation.

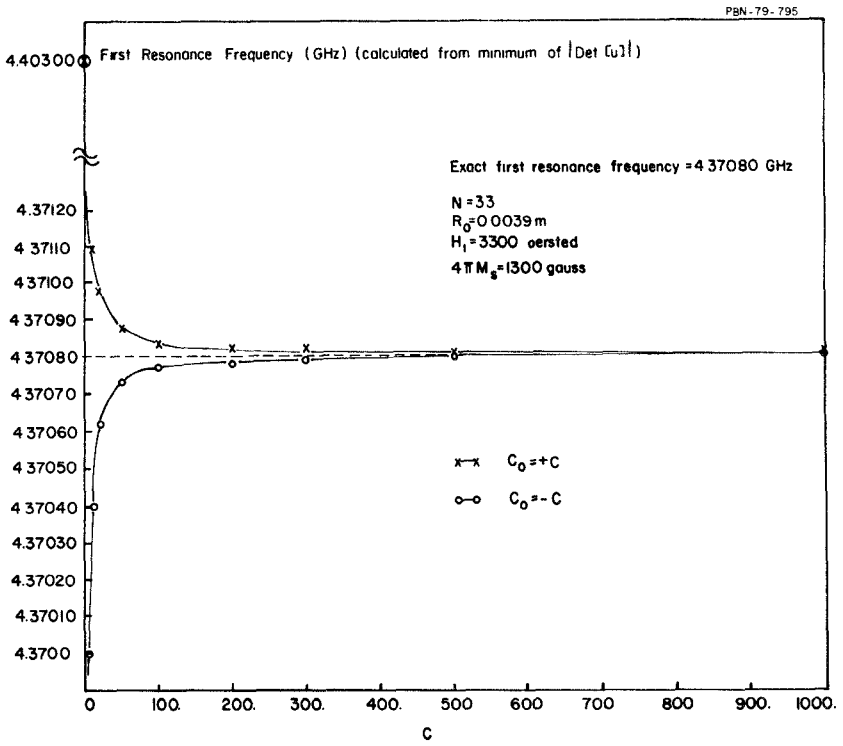

Fig. 12. Variation of the calculated first resonance frequency as the parameter C_0 is varied along the real axis.

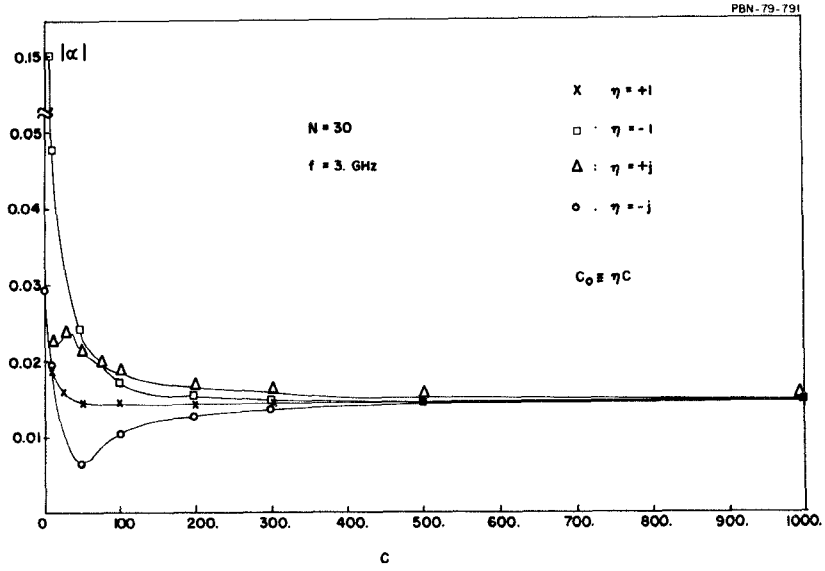

Fig. 13. Variation of $|\alpha|$ as the parameter C_0 is varied along the four axes in the complex C_0 plane for Ayter–Ayasli design and constant magnetic field boundary condition.

In the C_0 region where the results converge to a certain value, the numerical results should also be independent of N, the number of sampling points. This must be the case because if the matrix equations are modeling the integral equation properly, the physical results should not depend on N.

In Fig. 16, for Wu–Rosenbaum design and $C_0 = +300$, the circulator behavior is compared for two different values of N. The two sets of curves are in good agreement.

In Fig. 17, on the other hand, the same comparison is made for $C_0 = 0$. It is seen that the results for this value of C_0 do not converge for these two different N values.

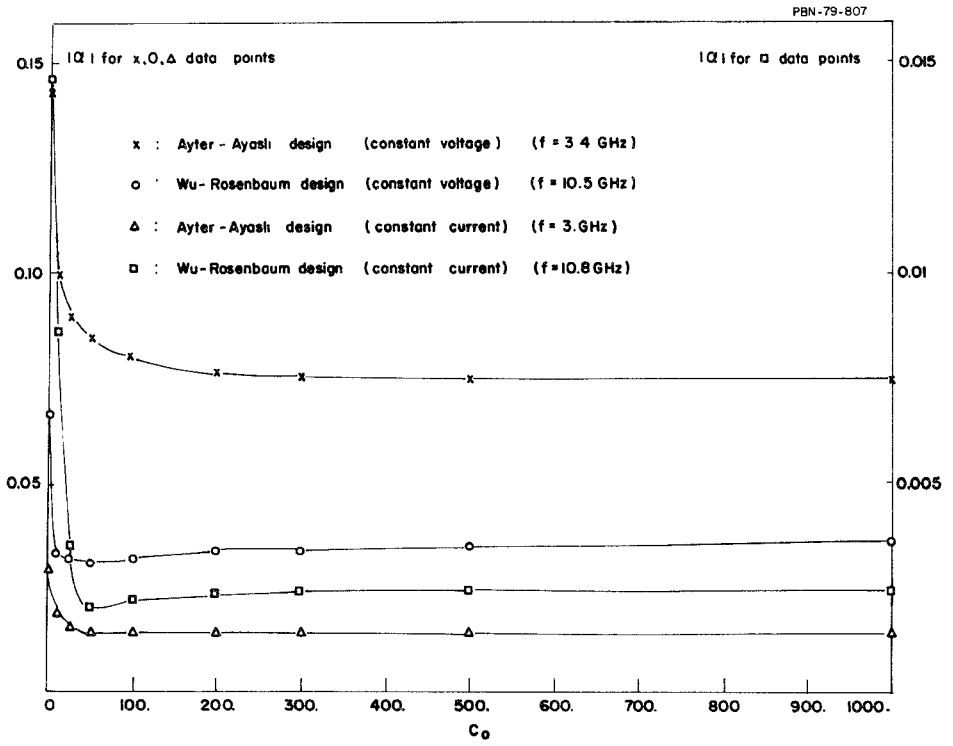

Fig. 14. Variation of $|\alpha|$ as the parameter C_0 is varied on the positive real axis for the four examples considered.

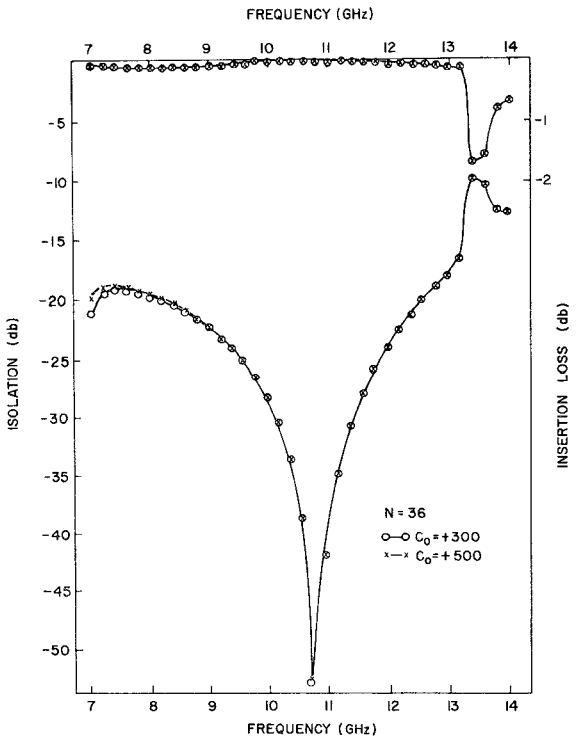

Fig. 15. Comparison of results for two different values of C_0 on Wu–Rosenbaum design with constant magnetic field boundary condition.

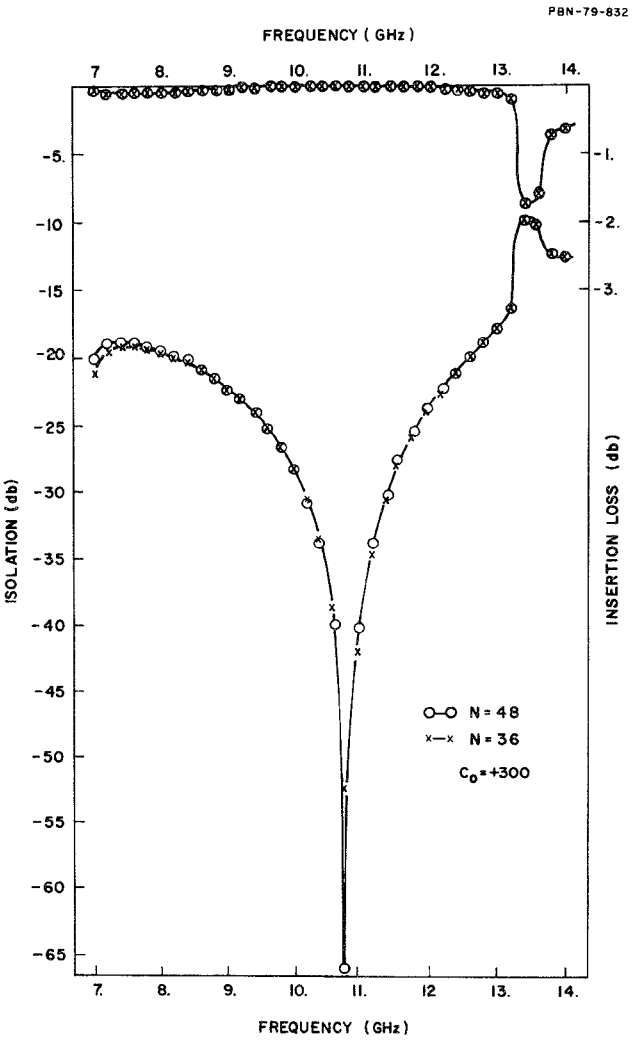

Fig. 16. Comparison of results on Wu–Rosenbaum design with constant magnetic field boundary condition for two different values of $N(C_0 = +300)$.

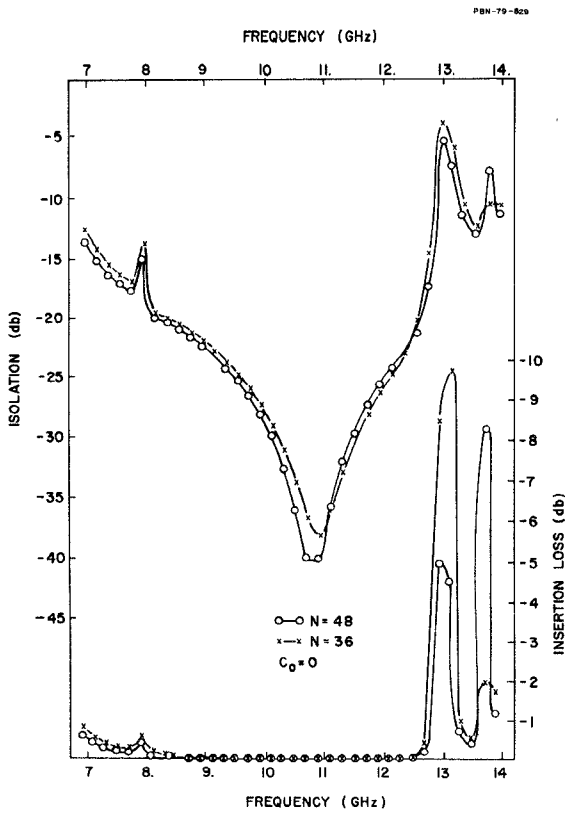

Fig. 17. Comparison of results on Wu–Rosenbaum design with constant magnetic field boundary condition for two different values of $N(C_0=0)$.

The effect of C_0 on the matrix stability is also investigated. The matrix condition numbers can be used to indicate regions of instability for the matrix equation system modeling the integral equation. In Fig. 18, the condition number calculated using the maximum norm [8] is plotted as a function of C_0 for the Ayter–Ayasli design.

The calculation of the condition number of a matrix requires explicit knowledge of its inverse. Another quantity which is claimed to give similar information on the condition of the matrix without requiring an explicit inverse is called the pivot ratio (PR) [9]. This quantity is defined as the ratio of the magnitudes of the first to the last pivot elements chosen in a Gaussian elimination procedure. The PR for the same example is also plotted on Fig. 18.

From Fig. 18, it is seen that the condition of the matrix equations deteriorates linearly with the parameter C_0. For this reason, C_0 should not be increased to values larger than necessary for the rapid convergence.

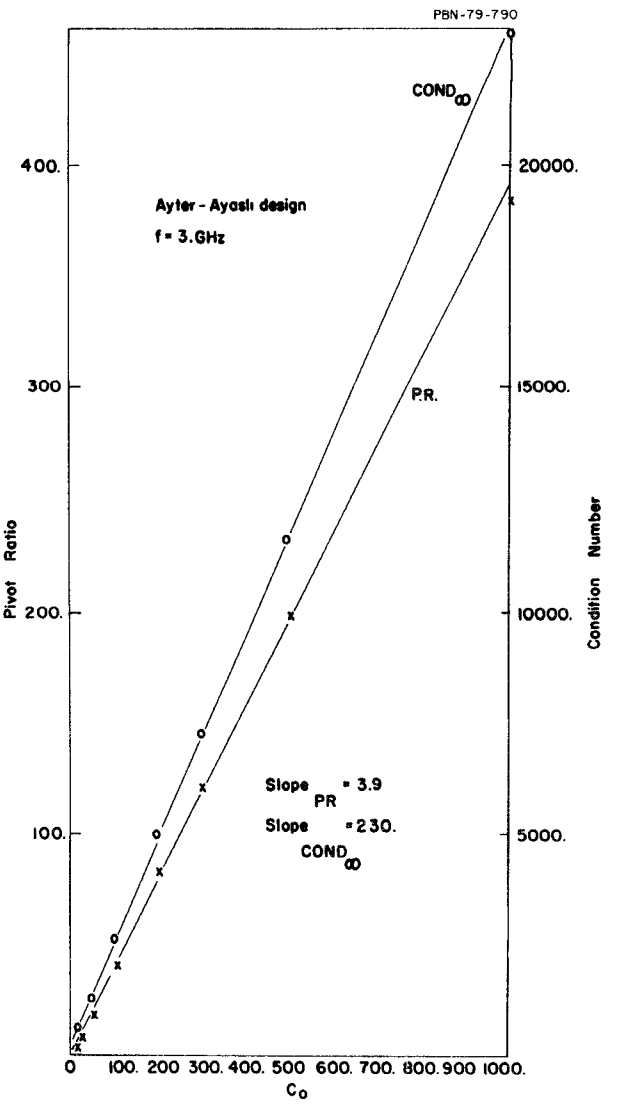

Fig. 18. Variation of the condition number (infinite norm) and PR as the parameter C_0 is varied along the positive real axis for Ayter–Ayasli design with constant magnetic field boundary condition.

Acknowledgment

The author wishes to thank Dr. Altunkan Hizal for helpful discussions on the numerical calculations.

References

[1] Y. S. Wu and F. J. Rosenbaum, "Wide-band operation of microstrip circulators," *IEEE Trans. Microwave Theory Tech.*, vol. MTT-22, pp. 849–856, 1974.

[2] S. Ayter and Y. Ayasli, "The frequency behavior of stripline circulator junctions," *IEEE Trans. Microwave Theory Tech.*, vol. MTT-26, pp. 197–202, March 1978.

[3] T. Miyoshi, S. Yamaguchi, and S. Goto, "Ferrite planar circuits in microwave integrated circuits," *IEEE Trans. Microwave Theory Tech.*, vol. MTT-25, pp. 593–599, 1977.

[4] T. Okoshi and T. Miyoshi, "The planar circuit—An approach to microwave integrated circuitry," *IEEE Trans. Microwave Theory Tech.*, vol. MTT-20, pp. 245–252, 1972.

[5] J. G. de Koning, R. J. Hamilton, and T. L. Hierl, "Full-band Low-loss continuous tracking circulation in K-band," *IEEE Trans. Microwave Theory Tech.*, vol. MTT-25, pp. 152–155, 1977.

[6] H. Bosma, "On the principle of stripline circulation," *Proc. IEEE Part B Supplement*, vol. 109, pp. 137–146, 1962.

[7] R. Mittra and T. Itoh, "Charge and potential distributions in shielded striplines," *IEEE Trans. Microwave Theory Tech.*, vol. MTT-18, pp. 149–156, 1970.

[8] G. E. Forsythe and C. B. Moler, *Computer Solution of Linear Algebraic Systems*. Englewood Cliffs, NJ: Prentice-Hall, 1967.

[9] R. Mittra and C. A. Klein, "The use of pivot ratios as a guide to stability of matrix equations arising in the method of moments," *IEEE Trans. Antennas Propagat.*, vol. AP-23, pp. 448–450, 1975.